ROBUST SPECTRAL UNMIXING OF MULTISPECTRAL LIDAR WAVEFORMS

Y. Altmann[(1)], *A. Maccarone*[(1)], *A. McCarthy*[(1)], *G. Newstadt*[(2)], *G. S. Buller*[(1)*], *S. McLaughlin*[(1)†], *A. Hero*[(3)‡]

[(1)] School of Engineering, Heriot-Watt University, Edinburgh, U.K.
[(2)] Google Inc., Pittsburgh, PA, U.S.A.
[(3)] Department of Electrical Engineering and Computer Science, University of Michigan, U.S.A.
Email: {Y.Altmann, am827, A.McCarthy, G.S.Buller, S.McLaughlin}@hw.ac.uk;
newstage37@gmail.com; hero@eecs.umich.edu

ABSTRACT

This paper presents a new Bayesian spectral unmixing algorithm to analyse remote scenes sensed via multispectral Lidar measurements. To a first approximation, each Lidar waveform consists of the temporal signature of the observed target, which depends on the wavelength of the laser source considered and which is corrupted by Poisson noise. When the number of spectral bands is large enough, it becomes possible to identify and quantify the main materials in the scene, on top of the estimation of classical Lidar-based range profiles. Thanks to its anomaly detection capability, the proposed hierarchical Bayesian model, coupled with an efficient Markov chain Monte Carlo algorithm, allows robust estimation of depth images together with abundance and outlier maps associated with the observed 3D scene. The proposed methodology is illustrated via experiments conducted with real multispectral Lidar data.

***Index Terms*—** Multispectral Lidar, Depth imaging, Robust spectral unmixing, Anomaly detection, Markov Chain Monte Carlo.

1. INTRODUCTION

Laser altimetry (or Lidar) is an acknowledged tool for extracting spatial structures from three-dimensional (3D) scenes. Using time-of-flight to create a distance profile, signal analysis can recover, for instance, tree and canopy heights, leaf area indices and ground slope by analyzing the reflected photons from a target. Conversely, passive multispectral (MSI) and hyperspectral images (HSI) are widely used to extract spectral information about the scene which can also provide useful parameters about the canopy composition and/or health. The most natural evolution to extract spatial and spectral information from sensed scenes is to couple Lidar data and multi/hyperspectral images [1, 2]. Although the fusion of Lidar data and HSIs can improve scene characterization, data synchronization issues in space (alignment, resolution) and time (dynamic scene, change of observation conditions, etc.) are still open issues. For these reasons, multispectral Lidar (MSL) has recently received attention from the remote sensing community for its ability to extract both structural and spectral information from 3D scenes [3–5]. The key advantage of MSL is the ability to potentially provide information on the full 3D distribution of materials, especially for scenes including semi-transparent objects (e.g., vegetation or fences). Another motivation for MSL is that HSI, even when fully synchronized, can only integrate the spectral response along the path of each optical ray, not measure the spectral response as a function of distance, e.g. depth into a forest canopy. In [5, 6], spectral unmixing techniques were developed to analyze 3D scenes composed of multi-layered objects, assuming that the spectral signatures of the materials composing the scenes were known and assuming linear mixing processes. In this paper we extend the method proposed in [5] to account for and identify possible deviations from the classical linear mixing model (LMM) used to estimate the amount/abundances of each endmember (assumed known) present in the scene. We assume that for each pixel, the photons emitted by the pulsed laser sources at different wavelength are reflected onto a single surface. This is typically the case for short to mid-range (up to dozens of meters) depth imaging where the divergence of the laser source(s) can be neglected.

Single-photon Lidar and thus MSL systems usually record, for each pixel/region of the scene, a histogram of time delays between emitted laser pulses and the detected photon arrivals. Due to the discrete nature of detected photons, Poisson noise models are more appropriate for single-photon MSL data than Gaussian noise models classically used when analysing HSIs. Due to the design of the proposed experiments (performed indoor here) and to simplify the estimation problem, we further assume that the ambient light and dark counts can be neglected. In this paper, we demonstrate the possibility of efficient 3D scene analysis by exploiting geometric and spectral information contained in MSL data (33 wavelengths ranging from 500nm to 820nm), under favourable observation conditions. However, the proposed method can be easily extended to more difficult observation conditions, as discussed in the conclusions of the paper.

Adopting a classical Bayesian approach, appropriate prior distributions are chosen for the unknown parameters of the model and the joint posterior distribution of these parameters is then derived. A Markov chain Monte Carlo (MCMC) method is used to generate samples according to the posterior of interest. This fully Bayesian approach allows a careful study of the estimation performance (through the derivation of measures of uncertainty). Although very interesting, algorithmic improvement in terms of computational complexity is out of scope of this paper and is worthy of more effort which we will report in future work.

The remainder of the paper is organized as follows. Section 2 introduces the observation model associated with MSL returns for a single-layered object to be analyzed. Section 3 presents the hierarchical Bayesian model associated with the robust spectral unmixing problem considered and the associated posterior distribution. Section 4 describes the MCMC method used to sample from the posterior of interest and subsequently approximate appropriate Bayesian

*Part of this work was supported by the EPSRC via grants EP/N003446/1, EP/K015338/1, EP/M01326X/1

†Part of this work was supported by the EPSRC via grant EP/J015180/1.

‡Part of this work was supported by DOE Consortium for Verification Technology DE-NA0002534.

estimators. Results of experiments conducted on real MSL data are shown and discussed in Section 5 and conclusions are finally reported in Section 6.

2. PROBLEM FORMULATION

This section introduces the observation statistical model associated with MSL returns for a single-layered object which will be used in Section 3 for robust spectral unmixing of MSL data. We consider a 4-D array $\mathbf{Y}$ of Lidar waveforms and of dimension $N_{\text{row}} \times N_{\text{col}} \times L \times T$, where N_{row} and N_{col} stands for the number of rows and columns of the regular spatial sampling grid (in the transverse plane), L is the number of spectral bands or wavelengths used to reconstruct the scene and T is the number of temporal (corresponding to range) bins. Let $\mathbf{y}_{i,j,\ell} = [\mathbf{Y}]_{i,j,\ell,t} = [y_{i,j,\ell,1}, \ldots, y_{i,j,\ell,T}]^T$ be the Lidar waveform obtained in the pixel (i,j) using the ℓth wavelength. The element $y_{i,j,\ell,t}$ is the photon count within the tth bin of the ℓth spectral band considered. Let $d_{i,j}$ be the position of an object surface at a given range from the sensor, whose spectral signature (observed at L wavelengths) is denoted as $\boldsymbol{\lambda}_{i,j} = [\lambda_{i,j,1}, \ldots, \lambda_{i,j,L}]^T$. According to [7,8] and assuming that the ambient illumination and dark photon counts can be neglected, each photon count $y_{i,j,\ell,t}$ is assumed to be drawn from the following Poisson distribution

$$y_{i,j,\ell,t} | \lambda_{i,j,\ell}, t_{i,j} \sim \mathcal{P}\left(\lambda_{i,j,\ell} g_{0,\ell}(t - t_{i,j})\right) \tag{1}$$

where $g_{0,\ell}(\cdot)$ is the photon impulse response whose shape can differ between wavelength channels and $t_{i,j}$ is the characteristic time-of-flight of photons emitted by a pulsed laser source and reaching the detector after being reflected onto a target at range $d_{i,j}$ ($d_{i,j}$ and $t_{i,j}$ are linearly related in free-space propagation). Moreover, the impulse responses $\{g_{0,\ell}(\cdot)\}$ are assumed to be known and can usually be estimated during the imaging system calibration. We further assume that the spectral signatures of the scene surfaces can be decomposed as linear mixtures of R known spectral signatures $\mathbf{m}_r$ (also referred to as endmembers and gathered in the matrix $\mathbf{M} = [\mathbf{m}_1, \ldots, \mathbf{m}_R]$) possibly corrupted by sparse anomalies, that is

$$\boldsymbol{\lambda}_{i,j} = \mathbf{M}\boldsymbol{a}_{i,j} + \mathbf{r}_{i,j}, \quad \forall i,j, \tag{2}$$

where $\boldsymbol{a}_{i,j} = [a_{i,j,1}, \ldots, a_{i,j,R}]^T$ contains the abundances of the R endmembers in the pixel (i,j) and $\mathbf{r}_{i,j} \in \mathbb{R}_+^L$ is a sparse anomaly vector. In a similar fashion to [9, 10], these anomalies or deviations to the LMM can be due to actual outliers/corrupted data, nonlinear spectral mixtures or intrinsic endmember variability. Note that due to physical considerations the unknown abundance vectors $\{\boldsymbol{a}_{i,j}\}_{i,j}$ are assumed to have positive entries. It is important to recall that in this work, we consider applications where the observed objects consist of a single visible surface per pixel. We do not consider cases where the photons can penetrate through objects (e.g., semi-transparent materials for which we would like to infer the internal composition) or be reflected onto multiple surfaces. This assumption allows the spectral unmixing problem to be reduced to a two spatial dimensions problem, which could be extended for distributed targets in future work (see Conclusion). The problem addressed in this paper consists of jointly estimating the range of the targets (for all the image pixels) and solving the robust spectral unmixing problem (e.g., estimating the abundance vectors and identifying the pixels corrupted by anomalies). The next section studies a new Bayesian model developed to solve the problem considered.

3. BAYESIAN MODEL

3.1. Likelihood

Assuming that the MSL waveforms $\mathbf{y}_{i,j} = \{y_{i,j,\ell,t}\}_{\ell,t}$ of a given pixel (i,j) result from the photons reflection onto a surface associated with the spectrum $\boldsymbol{\lambda}_{i,j}$, the likelihood associated with the pixel (i,j) can be expressed as $f(\mathbf{y}_{i,j}|\boldsymbol{\lambda}_{i,j}, t_{i,j}) = \prod_{\ell,t} f_{\mathcal{P}}(y_{i,j,\ell,t}; \lambda_{i,j,\ell} g_{0,\ell}(t - t_{i,j}))$, when assuming that the detected photon counts/noise realizations, conditioned on their mean in all channels/spectral bands are independent. Considering that the noise realizations in the different pixels are independent, the joint likelihood can be expressed as

$$f(\mathbf{Y}|\boldsymbol{\Lambda}, \mathbf{T}) = \prod_{i,j} f(\mathbf{y}_{i,j}|\boldsymbol{\lambda}_{i,j}, t_{i,j}), \tag{3}$$

where $\boldsymbol{\Lambda} = \{\boldsymbol{\lambda}_{i,j}\}_{i,j}$ and $\mathbf{T}$ is a matrix gathering the target ranges.

3.2. Prior distributions

In this work, we do not account for the potential spatial correlations between the target distances in neighbouring pixels of the scene. Thus, each target position is considered as a discrete variable defined on $\mathbb{T} = \{t_{min}, \ldots, t_{max}\}$, such that $1 \leq t_{min} \leq t_{max} \leq T$ (in this paper we set $(t_{min}, t_{max}) = (1, T)$) and assign the target ranges independent uniform priors $p(t_{i,j} = t) = 1/T', \forall t \in \mathbb{T}$, where $T' = \text{card}(\mathbb{T})$. Note that more informative priors could be used, e.g., to capture potential spatial correlations affecting the range profiles, as in [8]. However, when the number of spectral bands L considered and the number of detected photon are significant, the depth estimation does not require informative regularization (as the L bands are used to estimate $t_{i,j}$). For this reason and for paper length constraints, we simply consider uniform priors here.

The following classical conjugate gamma/inverse-gamma prior model

$$a_{i,j,r}|\theta_r \sim \mathcal{G}(a_{i,j,r}|1, \theta_r), \tag{4a}$$

$$\theta_r \sim \mathcal{IG}(\theta_r; \epsilon, \epsilon), \tag{4b}$$

is assigned to the unknown abundances, where θ_r controls the prior mean and variance of the abundances of the rth endmember and ϵ is fixed to $\epsilon = 10^{-2}$, yielding weakly informative prior models. Note that the hierarchical model (4) promotes abundance sparsity and assumes that the abundances of a given material share *a priori* similar statistical properties (through r_k) while being flexible enough to allow to wide range of abundance values. Note also that prior models promoting abundance spatial smoothness could also be used, in a similar fashion to [8].

As in [9, 10], the outliers are assumed to be sparse, i.e., for most of the pixels and spectral bands, the outliers are expected to be exactly equal to zero. To model the outlier sparsity, we factorize the outlier matrix as $\mathbf{r}_{i,j} = \mathbf{z}_{i,j} \odot \mathbf{x}_{i,j}$, where $\mathbf{z}_{i,j} = [z_{i,j,1}, \ldots, z_{i,j,L}]^T \in \{0,1\}^L$ is a label vector, $\mathbf{x}_{i,j} \in \mathbb{R}^L$ and $\odot$ denotes the Hadamard (term-wise) product. This decomposition allows one to decouple the location of the sparse components from their values. More precisely, $z_{i,j,n} = 1$ if an outlier is present in the ℓth spectral band of the pixel (i,j) with value equal to $r_{i,j,\ell} = x_{i,j,\ell}$. Assuming the potential anomalies *a priori* share the same statistical properties, we consider the following independent conjugate gamma priors

$$x_{i,j,\ell}|\alpha, \beta \sim \mathcal{G}(x_{i,j,\ell}; \alpha, \beta), \quad \forall i,j,\ell, \tag{5}$$

where (α, β) are arbitrarily fixed parameters (we set $(\alpha, \beta) = (2, 0.5)$ here from preliminary runs for brevity but these parameters could also be estimated by including them in the hierarchical Bayesian model).

For many applications, the locations of outliers are likely to be spectrally (e.g., water absorption bands) and/or spatially (weakly represented components, local nonlinear mixtures,...) correlated. An interesting way to take correlated outliers/nonlinear effects into account is to consider Markov random fields (MRF) to build a joint prior for the anomaly labels in $\mathbf{Z} = \{\mathbf{z}_{i,j}\}_{i,j}$. In this paper, we use the Ising model proposed in [10] for robust linear unmixing of HSIs to define the prior $f(\mathbf{Z})$ (this model is not detailed here for brevity and the interested reader is invited to consult [10] for discussions about the Ising model considered).

3.3. Joint Posterior distribution

From the joint likelihood and prior model specified in Sections 3.1 and 3.2, we can now derive the joint posterior distribution for $\mathbf{T}, \mathbf{A} = \{\boldsymbol{a}_{i,j}\}, \mathbf{Z}, \mathbf{X} = \{\mathbf{x}_{i,j}\}$ and $\boldsymbol{\theta} = [\theta_1, \ldots, \theta_R]^T$, given the observed waveforms $\mathbf{Y}$ and the value of the fixed hyperparameters $\boldsymbol{\Phi} = (\eta, \alpha, \beta)$. Using Bayes' theorem, and assuming prior independence between $\mathbf{T}$, $\mathbf{A}$, $\mathbf{X}$ and $\mathbf{Z}$, the joint posterior distribution associated with the proposed Bayesian model is given by
$f(\mathbf{T}, \mathbf{A}, \mathbf{Z}, \mathbf{X}, \boldsymbol{\theta} | \mathbf{Y}, \boldsymbol{\Phi})$

$$\propto f(\mathbf{Y}|\mathbf{T}, \mathbf{A}, \mathbf{Z}, \mathbf{X}) f(\mathbf{A}|\boldsymbol{\theta}) f(\mathbf{T}) f(\boldsymbol{\theta}|\epsilon) f(\mathbf{X}|\alpha, \beta) f(\mathbf{Z}) \quad (6)$$

4. ESTIMATION STRATEGY

The posterior distribution (6) models our complete knowledge about the unknowns given the observed data and the prior information available. To perform joint depth estimation and spectral unmixing of the MSL data, we use the following four Bayesian estimators: 1) the minimum mean square error estimator (MMSE) of the abundances, 2) the marginal maximum a posteriori (MMAP) estimator of target ranges, 3) the MMAP estimator of the anomaly labels and 4) conditionally on the estimated outliers location, the MMSE estimator of the anomaly values (in a similar fashion to [11]). Note that we use the MMAP estimators for the target ranges and labels, as this estimator is particularly adapted to estimate discrete parameters.

In order to approximate these estimators of interest, we adopt a fully Bayesian approach and consider a Markov chain Monte Carlo method to generate samples according to the joint posterior (6). More precisely, we use a Metropolis-within-Gibbs sampler (including Hamiltonian Monte Carlo (HMC) updates [12]) to generate sequentially the unknown parameters from their conditional distributions and the samples are then used to approximate the Bayesian estimators of interest (after having discarded the first samples associated with the burn-in period of the sampler).

As in [8], the depth parameters can be updated in a parallel manner by sampling from discrete (with finite supports) distributions. In a similar fashion to [10], sampling each label $z_{i,j,\ell}$ from its conditional distribution can be achieved by drawing in $\{0, 1\}$ with known probabilities. In our experiments we used a Gibbs sampler implemented using a colouring scheme such that many labels can be updated in parallel.Regarding the abundance updates, it can be shown that the $N_{\text{row}} N_{\text{col}}$ abundances vectors are a posteriori conditionally independent and can thus be updated independently (and thus in a parallel manner). It can also be shown that their conditional distributions, although non-standard, are log-concave and we use HMC updates to sample the abundances (as in [11]). Similarly, HMC updates are used to update the anomaly values in $\mathbf{X}$. Finally, using the conjugacy of (4a) and (4b), updating θ_r can be achieved by sampling from inverse-gamma distributions.

5. RESULTS

We propose comparing the performance of the proposed method to analyze the depth and spectral profiles of an approximately 5×5cm scene (see Fig. 1 (a)) composed of different objects made of polymer clay and mounted on a dark-grey backboard at a distance of 1.8m from a time-of-flight scanning sensor, based on time-correlated single photon counting (TCSPC). The 16 clay objects have been created by mixing 4 different clays (green, red, blue and orange) with known proportions (volume fractions). The transceiver system and data acquisition hardware used for this work is broadly similar to that described in [13,14], which was previously developed at Heriot-Watt University. The measurements have been performed indoor, in the dark to limit the influence of ambient illumination. The scene has been scanned using a regular spatial grid of 190×190 pixels and $L = 33$ regularly spaced wavelengths ranging from 500nm to 820nm. The histograms consist of $T = 3000$ bins of 2ps, which represents a depth resolution of 300μm per bin. The power of the supercontinuum laser source has been adjusted from preliminary runs and the per-pixel acquisition time is 10ms for each wavelength. The instrumental impulse responses $g_{0,\ell}(\cdot)$ were estimated from preliminary experiments by analyzing the distribution of photons reflected onto a Spectralon panel (a commercially available Lambertian scatterer). The proposed algorithm has been applied with $N_{\text{MC}} = 5000$ sampler iterations (including $N_{\text{bi}} = 2000$ burn-in iterations). Fig. 1 (b) shows the estimated depth/range image which is in very good agreement with the structure of the scene in Fig. 1 (a) (the reference range being set to the range of the backboard).

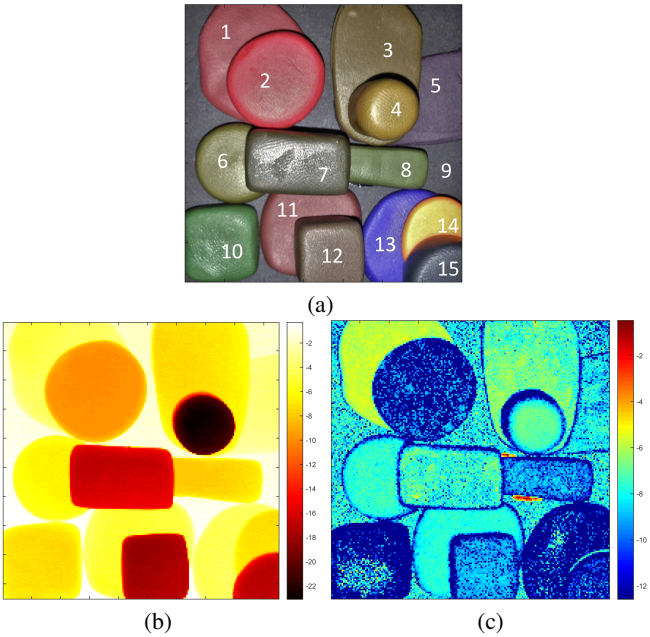

(a)

(b) (c)

Fig. 1. (a): Standard RGB image of the scene composed of different coloured clays fixed on a dark-grey backboard. (b) Estimated depth/range image in millimetre (the reference range corresponds to the backboard range). (c) Anomaly map ($\log(\|\mathbf{r}_{i,j}\|^2 / L)$) associated with the region of interest.

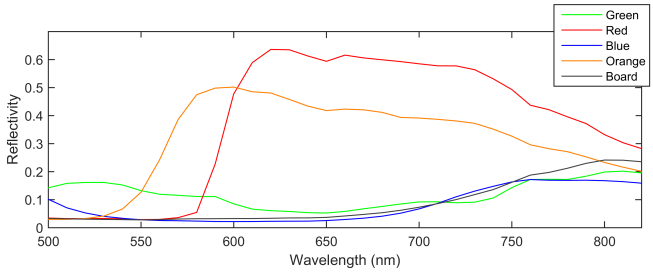

Fig. 2. Spectral signatures of the backboard and the 4 polymer clays (green, red, blue and orange) mixed to create the objects of the scene.

Fig. 2 shows the spectral signatures of the backboard and the 4 kinds of clay used to create the objects. This figure highlights the fact that the blue clay and the backboard have low reflectances and present very similar profiles from 550nm to 750nm, which makes the unmixing problem particularly difficult.

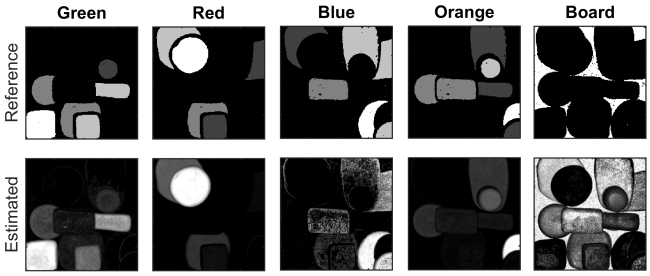

Fig. 3. Top: reference abundances (computed from volume fractions for mixtures of clays) associated with the $R = 5$ main materials composing the scene. Bottom: Abundance maps estimated by the proposed method (all images have the same dynamic, i.e., between 0 and 1).

Fig. 3 compares the estimated abundances to the reference mixing coefficients (volume fractions) used to create the scene. The estimated abundances are generally in good agreement with the reference images as it is possible to identify the regions where the different clays are present. However, significant difference appear in the blue clay and backboard abundances maps, mainly due to the reasons mentioned above. Note also that the reference volume fractions do not necessarily translate directly into the abundances involved in the spectral mixtures, (which is why the top sub-images of Fig. 3 are referred to as reference and not ground truth). This can explain the difference between the reference and estimated maps. It is important to recall that the unmixing process, although combined with a depth estimation strategy, does not explicitly use depth information to enhance the abundance estimation. Consequently, the proposed algorithm provides similar results when the targets are at the same or different distances from the imaging system. For completeness, Fig. 4 depicts the spectral responses of the 15 main materials identified in Fig. 1 (a) and obtained via spectral classification [15]. Finally, Fig. 1 (c) shows the estimated anomaly map. This figure highlights a first region of significant deviations from the classical LMM, in the central region of the scene (two horizontal stripes around the material #8). These deviations (high reflectivities between 750nm and 820nm) correspond to the presence of residual glue used to fix the clay objects on the backboard. The second region of less significant deviations (material #1) are detected between 500nm and 550nm and might be due to nonlinear mixing effects. Indeed these effects can also be observed less clearly in the top right corner of the scene

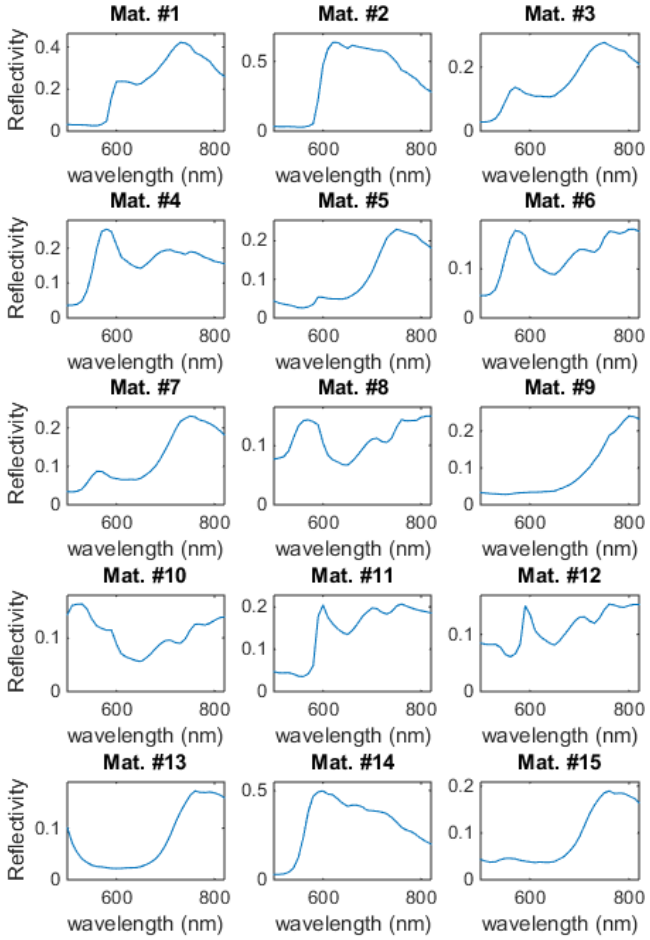

Fig. 4. Estimated spectral signatures of 15 materials identified in Fig. 1 (a).

(mixture of orange and blue clays). It seems reasonable to think that the remaining regions, of lower anomaly levels, are mainly affected by the spectral variability of the materials considered.

6. CONCLUSION

We proposed a new Bayesian model and a joint depth estimation and robust spectral unmixing algorithm for 3D scene analysis from MSL data. Assuming the ambient illumination can be neglected, the spectra of the scene surfaces visible by the imaging system were decomposed into linear mixtures of known endmembers, potentially corrupted by sparse deviations/anomalies. Adopting a Bayesian approach, prior distributions were assigned to the unknown model parameters; in particular, a 3D Ising model was used to model the spatial organization of the anomalies. Including ambient illumination and dark count levels in the observation model (as in [8, 14, 16, 17]) is the obvious next step from a more general application (especially for long-range imaging applications) of the proposed method. In future work, and especially for remote sensing applications, it will be crucial to account for the presence of distributed (multi-layered) targets, which would yield multiple returns in the MSL data. This could potentially allows the estimation of real 3D abundance profiles

7. REFERENCES

[1] M. Dalponte, L. Bruzzone, and D. Gianelle, "Fusion of hyperspectral and lidar remote sensing data for classification of complex forest areas," *IEEE Trans. Geosci. and Remote Sensing*, vol. 46, no. 5, pp. 1416–1427, May 2008.

[2] Simon J. Buckley, Tobias H. Kurz, John A. Howell, and Danilo Schneider, "Terrestrial lidar and hyperspectral data fusion products for geological outcrop analysis," *Computers & Geosciences*, vol. 54, pp. 249–258, 2013.

[3] A. M. Wallace, C. J. Nichol, and I. H. Woodhouse, "Recovery of forest canopy parameters by inversion of multispectral lidar data," *Remote Sensing*, vol. 4, no. 2, pp. 509–531, 2012.

[4] T. Hakala, J. Suomalainen, S. Kaasalainen, and Y. Chen, "Full waveform hyper-spectral lidar for terrestrial laser scanning," *Opt. Express*, vol. 20, no. 7, pp. 7119–7127, Mar 2012.

[5] Y. Altmann, A. Wallace, and S. McLaughlin, "Spectral unmixing of multispectral lidar signals," *IEEE Trans. Signal Process.*, vol. 63, no. 20, pp. 5525–5534, Oct. 2015.

[6] A. M. Wallace, A McCarthy, C.J. Nichol, Ximing Ren, S. Morak, D. Martinez-Ramirez, IH. Woodhouse, and G. S. Buller, "Design and evaluation of multispectral lidar for the recovery of arboreal parameters," *IEEE Trans. Geoscience and Remote Sensing*, vol. 52, no. 8, pp. 4942–4954, Aug 2014.

[7] S. Hernandez-Marin, A. M. Wallace, and G. J. Gibson, "Bayesian analysis of lidar signals with multiple returns," *IEEE Trans. Patt. Anal. Mach. Intell.*, vol. 29, no. 12, pp. 2170–2180, Dec 2007.

[8] Y. Altmann, X. Ren, A. McCarthy, G. S. Buller, and S. McLaughlin, "Lidar waveform based analysis of depth images constructed using sparse single-photon data," *IEEE Trans. Image Processing*, 2016, to appear.

[9] Gregory E. Newstadt, Alfred Hero III, and Jeff Simmons, "Robust spectral unmixing for anomaly detection," in *Proc. IEEE-SP Workshop Stat. and Signal Processing*, Gold Coast, Australia, July 2014.

[10] Y. Altmann, S. McLaughlin, and A. Hero, "Robust linear spectral unmixing using anomaly detection," *IEEE Trans. Comput. Imaging*, vol. 1, no. 2, pp. 74–85, June 2015.

[11] Y. Altmann, N. Dobigeon, and J. Tourneret, "Unsupervised post-nonlinear unmixing of hyperspectral images using a hamiltonian monte carlo algorithm," *IEEE Trans. Image Processing*, vol. 23, no. 6, pp. 2663–2675, June 2014.

[12] S. Brooks, *Handbook of Markov Chain Monte Carlo*, Chapman & Hall/CRC Handbooks of Modern Statistical Methods. Taylor & Francis, 2011.

[13] A. McCarthy, X. Ren, A. Della Frera, N. R. Gemmell, N. J. Krichel, C. Scarcella, A. Ruggeri, A. Tosi, and G. S. Buller, "Kilometer-range depth imaging at 1550 nm wavelength using an InGaAs/InP single-photon avalanche diode detector," *Opt. Express*, vol. 21, no. 19, pp. 22098–22113, Sept. 2013.

[14] Y. Altmann, X. Ren, A. McCarthy, G. S. Buller, and S. McLaughlin, "Target detection for depth imaging using sparse single-photon data," in *Proc. IEEE Int. Conf. Acoust., Speech, and Signal Processing (ICASSP)*, Shanghai, China, 2016, to appear, technical report available online, http://yoannaltmann.weebly.com/publications.html.

[15] Y. Altmann, A. Maccarone, A. McCarthy, G. S. Buller, and S. McLaughlin, "Joint range estimation and spectral classification for 3d scene reconstruction using multispectral lidar waveforms," in *Proc. IEEE-SP Workshop Stat. and Signal Processing*, Palma de Mallorca, Spain, June 2016, to appear.

[16] A. Kirmani, D. Venkatraman, D. Shin, A. Colao, F. N. C. Wong, J. H. Shapiro, and V. K. Goyal, "First-photon imaging," *Science*, vol. 343, no. 6166, pp. 58–61, 2014.

[17] Dongeek Shin, A. Kirmani, V.K. Goyal, and J.H. Shapiro, "Computational 3d and reflectivity imaging with high photon efficiency," in *Proc. IEEE Int. Conf. Image Processing (ICIP)*, Oct. 2014, pp. 46–50.